Channel Modeling and Characteristics of Human Motion Using Dynamic Ray Tracing and MoCap

Yuan Liu, Johann Fuchs, M. R. Bhavani Shankar
Interdisciplinary Centre for Security, Reliability and Trust (SnT), University of Luxembourg, L-1855, Luxembourg
Email: {yuan.liu, johann.fuchs, bhavani.shankar}@uni.lu

***Abstract*—Radio-based motion behavior recognition is a key to enabling integrated sensing and communication (ISAC) in the 6G landscape. Data-driven approaches are popular to achieve human motion identification and most of them are based on the range-Doppler maps (RDMs) of radar measurements, where the Doppler and the micro-Doppler (uDop) frequency shifts due to motion are embedded. In this paper, we characterize the human motions of the radar signals using typical wireless channel modeling parameters, e.g., normalized Doppler power spectral density (ND-PSD) and root-mean-square Doppler spread (RMS-DS). Specifically, a proposed dynamic ray tracing (RT) based on Blender is used to simulate time-varying radar channels, where the real human motions are imported from the motion capture (MoCap) database, hence the simulated radar channels contain dynamic real human motion, multipaths of clutters, and also the interaction between target and the environment. The simulation results show that the Doppler channel parameters are consistent with the conventional radar images, besides containing more semantic information about the human motions and scenarios. This provides the feasibility of utilizing channel parameters as training datasets.**

***Index Terms*—Channel modeling, channel parameters, FMCW radar, human motion recognition, dynamic ray tracing.**

I. Introduction

The emerging integrated sensing and communication (ISAC) technology is believed to be a key vertical in the 6th generation (6G) communication era. The use of millimeter wave (mmWave) and terahertz (THz) technology in 6G will offer radio-based sensing sufficient resolution and accuracy in indoor applications [1], [2], e.g., monitoring assisted living, where privacy is paramount [3].

Many of the human-centric sensing applications benefit from the fact that human limbs move differently from the torso for different applications, thereby generating characteristic micro-Doppler (uDop) and Doppler frequency shifts, respectively [4]. Typically, data-driven-based approaches are trained using the time-varying Doppler and uDop signatures to exploit these characteristics and to realize behavior identification and gesture classification. For example, [5] and [6] deploy the continuous range-Doppler maps (RDMs) of frequency-modulated continuous wave (FMCW) radar in eating gesture detection, and classifying human motions, respectively. However, there are two shortcomings in using RDMs to characterize human activities. Firstly, these radar images have range-angle-velocity ambiguities that are dependent on waveforms [7], [8]. Secondly, many radar image-based training works usually ignore the multipath effects due to the environment, e.g., [6], while the ghost targets due to multipath can fade the uDop features in realistic indoor measurement.

Physics-based channel modeling is another approach to characterizing human activities. Different from the radar images, these channel parameters are not constrained to specific waveforms. These channel parameters include amplitude, range, and Doppler frequency shift for the different paths, thereby inherently incorporating the multipath. The statistical description of the parameters reveals features of channel fingerprint [9], which has been used in data-driven approaches for indoor localization [10] and outdoor environment identification [11]. Typically, the training is twofold. Firstly, the high-resolution parameter estimation (HRPE) algorithm, e.g., space-alternative generation expectation-maximization (SAGE) [10], is utilized to estimate each of the multipath. Subsequently, the channel features are calculated and networks are trained. However, estimating Doppler parameters of large-scale scenarios using HRPE has been undertaken in [12], while estimating the uDop components of human motion is challenging. Because there are more multipaths in indoor scenarios, while the multipaths resulting in uDop are typically weak. Further, the use of measured data to model the features of indoor human motion requires HRPE algorithms working in low signal-noise ratios (SNRs). In contrast, the dynamic ray tracing (RT) simulator can provide the exact parameters of each multipath based on the built environment and human motions [13].

To the best of the authors' knowledge, utilizing channel parameters like Doppler and uDop for human motion modeling is not well investigated. In this paper, we modify the dynamic RT channel [13] to be a hybrid of scattering and mirror-reflecting paths to account for multipath. Subsequently, we simulate the dynamic channels of five representative human walking movement scenarios and characterize the time-varying motions using parameters common in wireless channels, i.e., normalized Doppler power spectral density (ND-PSD) and root-mean-square Doppler spread (RMS-DS) [12]. Further, we analyze these channel parameters for different motions and detail the influence of indoor clutter and ghost targets. Finally, the characterized time-varying channel parameters of different motions are compared with the conventionally used time-Doppler maps.

This research was funded in whole by the Luxembourg National Research Fund (FNR) through the BRIDGES project MASTERS under grant BRIDGES2020/IS/15407066.

The hybrid dynamic RT codes are available https://gitlab.com/yuan.liu1/hybriddynamicrt.

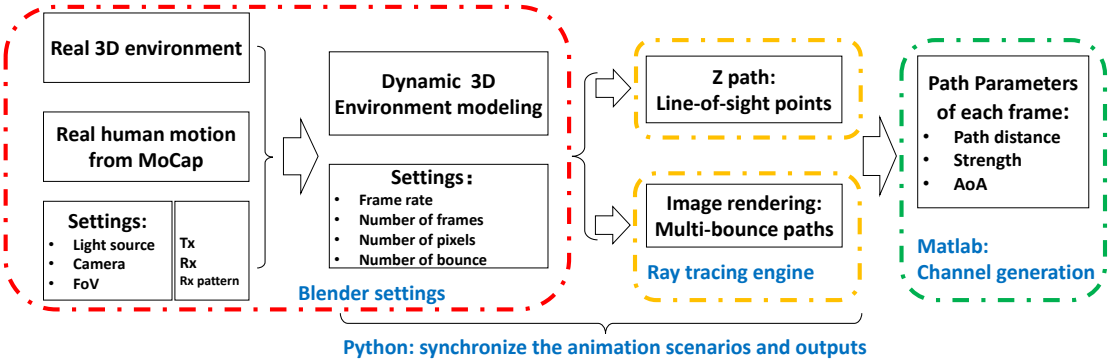

Fig. 1. The outline of the dynamic RT simulation.

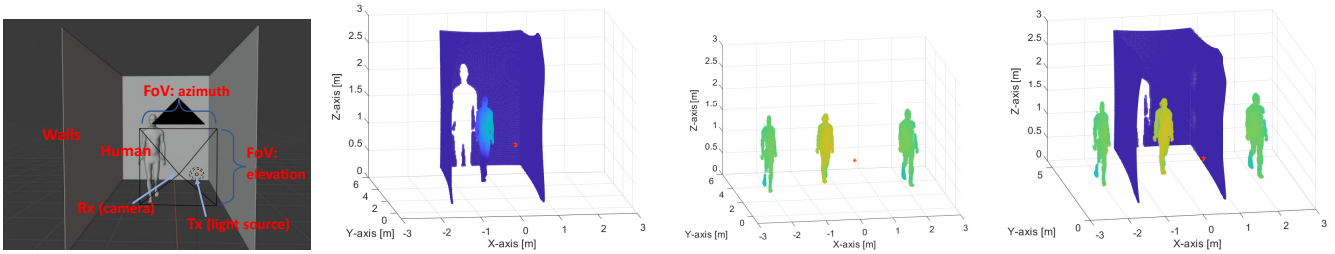

(a) 3D scenario (b) Scattering point clouds (c) Reflecting point clouds (d) Composite point clouds

Fig. 2. Visualization of multipaths using point clouds.

II. Dynamic RT simulation

We modify the Blender-based dynamic simulation set-up proposed in [13] to generate human motion channels. Blender is an open-source 3-dimensional (3D) modeling tool, where dynamic animations of the environment can be built. Each frame of the dynamic animation is rendered into a number of pixels, where each pixel is regarded as a point scatterer/reflector. Then, by setting the locations of the transmitter (Tx) and receiver (Rx), parameters of the multipath propagation among the Tx, Rx, and the scattering points, e.g., distance, path strength, AoA, and Doppler shift of each path are calculated by the RT engine. Finally, these parameters are used to generate the radar channel.

To model the characteristics of human-centric motions in this application, we trigger the simulation in a hybrid way, i.e., the Z-path in Blender is used to generate the scattering paths, and the image-rendering based RT is used to simulate the mirror reflection of the human target. The outline of dynamic RT simulation is summarized in Fig. 1. The details of importing real human motions from the motion capture (MoCap) database and the hybrid multipath simulation will be elaborated in the sequel. Readers interested in further details regarding Fig. 1, can kindly refer to [13].

A. Realistic human motions

The MoCap database can provide realistic human (or other creature) motions of daily activities, originally created to optimize robotic applications. They use marker-based methods and inertial sensors to record human body motions, using high-resolution cameras to track the markers and collect skeletal velocities. For example, the KIT human motion database [14], combines a marker with inertial sensors and even records movements of finger joints during human activities. In our case, we use AMASS [15], an archive containing 15 different MoCap databases and up to 11265 realistic motion sequences, including the KIT database. In our applications, human motions are imported into Blender using an add-on introduced in [16] to create dynamic 3D scenarios, so that the propagation channel of human activities can be simulated under any environment. Further, it is possible to vary the human models for all MoCap shots, e.g. heights and shapes can be configured, providing further variation to expand the available datasets. MoCap is environment-free, hence the combination of MoCap and 3D modeling makes it possible to quickly and easily generate large amounts of channel data for different scenarios. A snapshot example of a human walking in the corridor is shown in Fig. 2a, where the Tx and Rx are colocated, the Tx is omnidirectional, and the Rx is assumed to have uniform gain in the field of view (FoV) of the camera used in Blender.

B. The hybrid ray tracing

The RT engine in Blender can simulate the multi-bounce paths, i.e., the paths bouncing among targets/environment more than once, with the consideration of all the propagation mechanisms based on the roughness of the material surfaces of the 3D environment, i.e., scattering, reflection, diffraction, and transmission [17]. The wave propagation depends on the frequency band, materials, and the roughness of the surfaces of humans and environments. Since the Blender simulation is based on light waves, using it in radio simulation requires proper modeling and calibration. Hence, the novelty of the imaging-based approach in the previous work [13] lies in

the geometrical parameter simulations in dynamic scenarios, especially the Doppler frequency shift.

In this human-centric motion characterization, we propose the hybrid simulation approach, i.e., calculate the scattering path channel and the reflecting path channel separately.

Scattering paths: The Blender can output the Z-path of each pixel, i.e., the exact distance from each pixel (point-target) to the camera. We utilize the Z-path outputs as the scatterers, and the reconstructed point clouds are shown in Fig. 2b[1].

Reflecting paths: We set the walls to be smooth reflectors, hence the interaction between targets and the wall are only reflection paths. Using the image-rendering-based RT in [13], the outputs of the reflecting paths are visualized as point clouds in Fig. 2c, where the mirror targets due to reflections of the left and the right walls are shown, respectively. The mirror target is also well known as the ghost target in radar systems.

Composite channel: The overall channel is a composition of scattering and reflecting components, where the points that contribute to both reflection and scattering paths, are shown in Fig. 2d.

C. Dynamic signal generation

Once the information from the point clouds is gathered from the Blender (refer [13] for details), the radar signal for the FMCW transmissions is generated. While [13] deals only with the generation of multi-bounce paths based on the image-rendering approach, this paper extends these calculations to the proposed hybrid paradigm.

Considering a received signal of the beat-sampled time division multiplexing (TDM) FMCW signals $\mathbf{Z} \in \mathbb{C}^{L\times N_s}$, where N_s denotes the number of samples per chirp, and L denotes the number of chirps in one coherent processing interval (CPI). $n_s = 1, 2, ..., N_s$ and $l = 1, 2, ..., L$ denote the index of the samples and chirps, respectively, the (n_s, l)-th entry is the superposition of reflecting paths and scatterings paths as[2]

$$\mathbf{Z}(n_s,l) = \sum_{l_s=1}^{N_{\text{pi}}} S_{l_s} e^{j2\pi\left(\frac{2\mu R_{l_s}}{c}\frac{n_s-1}{F_s} - 2\frac{f_l v_{l_s}}{c}(l-1)\frac{T_f}{L} + \phi_{l_s}\right)} + \sum_{l_r=1}^{N_{\text{pi}}} S_{l_r} e^{j2\pi\left(\frac{2\mu R_{l_r}}{c}\frac{n_s-1}{F_s} - 2\frac{f_l v_{l_r}}{c}(l-1)\frac{T_f}{L} + \phi_{l_r}\right)}, \tag{1}$$

where $l_s = 1, 2, ..., L_{\text{pi}}$ and $l_r = 1, 2, ..., L_{\text{pi}}$ denote the indices of the scattering paths and reflecting paths, respectively, L_{pi} is the number of pixels defined in Blender, f_l is the carrier frequency, $\mu = B/T_p$ is the FMCW slope with B represents the bandwidth, T_p represents one chirp duration, c is light speed, F_s is the sampling frequency, T_f is the interval of two frames defined in Blender, ϕ_{l_s} and ϕ_{l_r} are random phase component, S_{l_s} and S_{l_r} are amplitudes of the scattering path and reflecting path, respectively, which include the scattering/ reflection coefficient and propagation attenuation, R_{l_s} and R_{l_r} are ranges of the scattering path and reflecting path, respectively, v_{l_s} and v_{l_r} are radial velocities of the scattering path and reflecting path, respectively.

The distance parameters R_{l_s} and R_{l_r} are obtained directly from the RT simulation via Z-path and image rendering, respectively, as shown in the simulation framework of Fig. 1. The radial velocity parameters v_{l_s} and v_{l_r} are calculated based on the differential of distance parameters. The path strength S_{l_s} and S_{l_r} can be obtained by the RT simulation, or calculated based on the radar equations using the distance parameters and proper scattering coefficients, for more details on obtaining multipath parameters refer to [13].

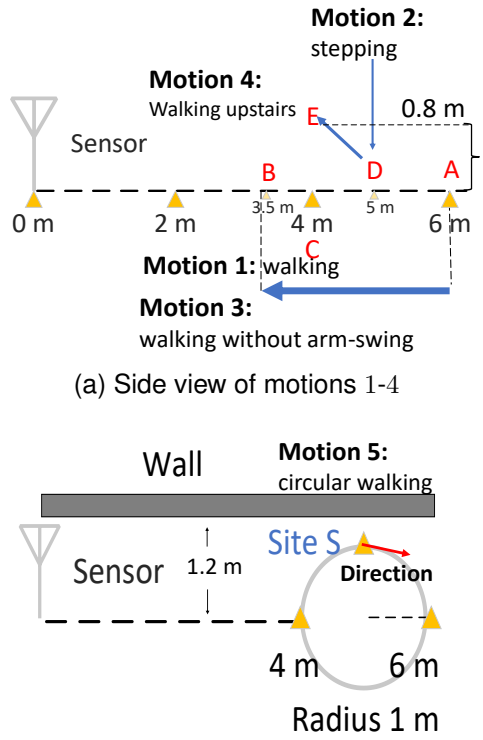

Fig. 3. Illustration of the simulated motions and scenarios.

III. Simulation and Discussion

This section first characterizes the different human motions illustrated in Fig. 3 and then explores the effects of scattering paths and reflecting ghosts. All these five motions including start, moving, and stop three stages.

The comparisons of motions 1 to 4 are in the anechoic chamber, we simulate four different walking motions and characterize the Doppler and uDop channel features. In the anechoic chambers, the multipath contains only the scattering paths from the human. The Doppler frequency shifts of the

[1]The outputs of multipaths are not point clouds. As described in Fig. 1, they are parameters of each multipaths. Based on the distance and AoA of each path, we can visualize the scatterers/reflectors as a one-bounce path and hence reconstruct the point clouds.

[2]In this paper, we concentrate on range-Doppler simulations, hence we ignore the phase shift among array elements in (1). Completed MIMO simulations are provided in [13].

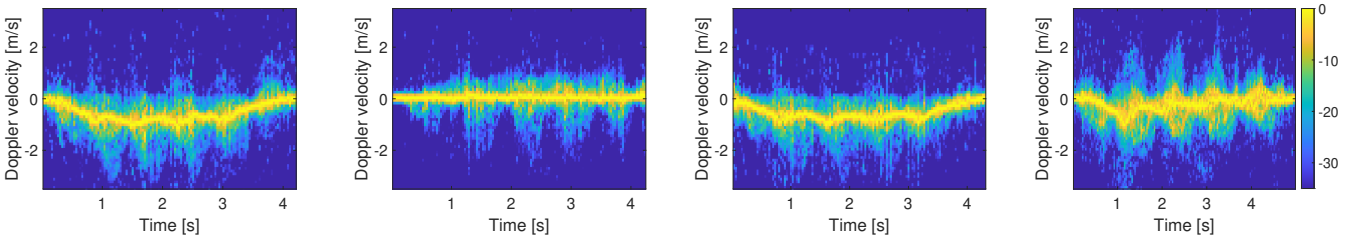

(a) Motion 1: time-Doppler (b) Motion 2: time-Doppler (c) Motion 3: time-Doppler (d) Motion 4: time-Doppler

Fig. 4. Time-Doppler results of motion 1 to motion 4, i.e., walking, stepping, walking without arm-swing, and walking upstairs, respectively.

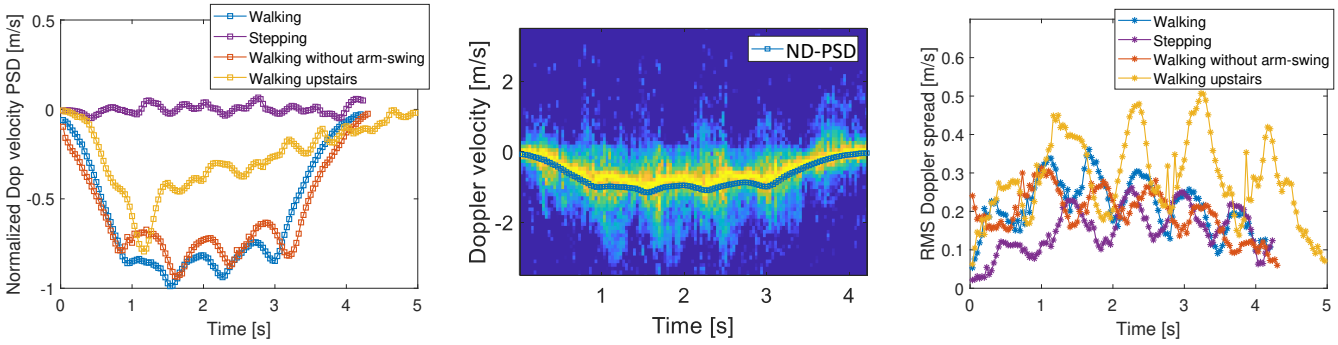

(a) Motions 1 to 4: ND-PSD (b) ND-PSD V.S. time-Doppler (c) Motions 1 to 4: ND-PSD

Fig. 5. Doppler PSD and RMS Doppler spread of motions 1 to 4.

TABLE I
SIMULATION CONFIGURATIONS

Contents	Configurations
Radar type	Monostatic
Central frequency [GHz]	77
Bandwidth [GHz]	3.6
FMCW slope [MHz/us]	60
Frame/CPI duration [ms]	40
NO. of chirps per frame	128
Sampling rates [MHz]	10
NO. of samples per chirp	256
Sensor height [meter]	1.2
Walk speed [m/s]	[0.75, 1]
Camera FoV [deg]	75
Motion 1	Walking
Motion 2	Stepping
Motion 3	Walking without arm-swing
Motion 4	Walking upstairs
Motion 5	Walking along a circle

multipath due to limbs and torso vary across the motions, enabling their characterization. As shown in Fig. 3a, motions 1 and 3 involve a straight walk towards the radar from spot A to B, covering a distance of 2.5 meters. Note that motion 1 refers to normal walking (with arms swinging) while there is no arm swing in motion 3. Motion 2 is stepping at the spot D, which is 5 meters away from the radar. Motion 4 is walking upstairs, from spot D to E, where the horizontal movement is around 1 meters and the vertical movement is around 0.8 meters. In the comparison of motion 5, we compare the effects due to scattering paths and reflecting mirror targets, respectively. The motion 5 is shown in Fig. 3b, where the human walks circularly in front of the sensor, where the distance is 5 meters and the radius is 1 meters, and a wall on the left of the walking track is considered in the simulation. The simulation configurations are listed in Tab. I.

A. *Quantification of walking motions*

The conventional time-Doppler results of motion 1 to 4 are shown in figures of Fig. 4a to Fig. 4d, respectively. The clear Doppler frequency shifts due to the torso's velocity are observed and match the actual motions. For example, in motion 1 and 3, the human walks towards the sensor, hence the Doppler of the torso's velocity is similar. In the stepping of motion 2, we observe almost zero Doppler of the torso. In motion 4, the subject walks upstairs. Since the measured radial velocity by the radar is the projection of the product of actual velocity and the cosine of the elevation angle, the radial velocity decreases as the human gains elevation. However, uDops of the four different motions are not well distinguished. Those four walking motions give a similar uDop from the conventional time-Doppler results. To give quantified evaluations of the Doppler component analysis, we apply the channel parameters ND-PSD and RMS-DS [12] to quantify and characterize the human motions[3].

The ND-PSD of the ith chirp is defined as

$$D_i(v) = \frac{\sum_{l_i} |S_{l_i}|^2 \delta(v - v_{l_i})}{\sum_{l_i=1} |S_{l_i}|^2}, \tag{2}$$

[3]Doppler frequency shift is denoted by the term $\frac{-2f_l v_l}{c}$ in (1), here we use Doppler velocity v_l for calculation.

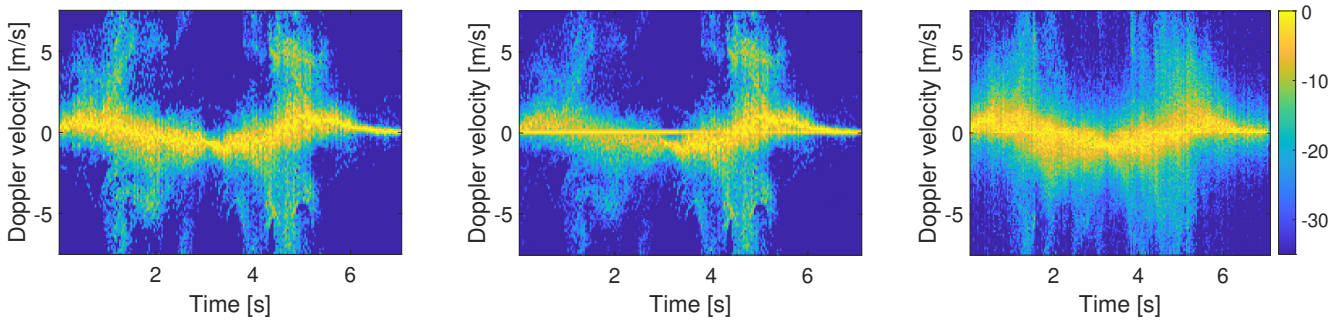

Fig. 6. Time-Doppler results of circular walking under three environment scenarios.

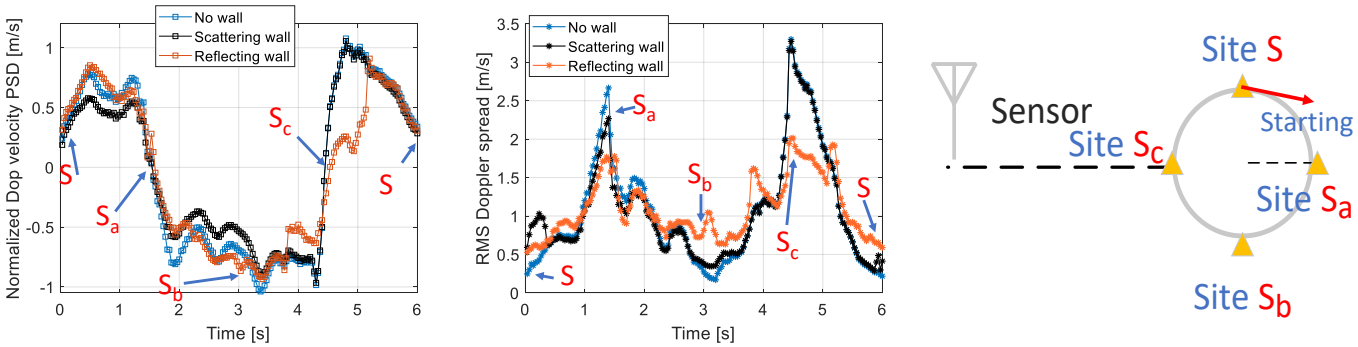

Fig. 7. Doppler PSDs, RMS DSs, and illustration of the walking track of motion 5.

where l_i denotes the index of the multipath, S_{l_i} and v_{l_i} denote the amplitude and Doppler velocity of the l_ith path in the channel. The ND-PSD denotes the amplitude-weighted mean Doppler velocity of all multipaths in a channel, i.e., the human's radius velocity in this application. The ND-PSDs of the four motions are shown in figures of Fig. 5a, i.e., the velocity of the torsos are shown, which are exactly with the strongest Doppler curves in Fig. 4. For example, a comparison of the ND-PSD and time-Doppler map of motion 1 is shown in Fig. 5b, which validates our assumption.

The second moment of the Doppler velocity is

$$\mathbb{E}_i[v^2] = \frac{\sum_{l_i=1} |S_{l_i}|^2 v_{l_i}^2}{\sum_{l_i=1} |S_{l_i}|^2}, \tag{3}$$

and the RMS-DS is defined as

$$R_i = \sqrt{\mathbb{E}_i[v^2] - \mathbb{E}_i[v]^2}. \tag{4}$$

The RMS-DS denotes the amplitude-weighted variance of the Doppler velocity of all multipaths in the channel, i.e., the uDop in this application. The RMS-DSs of the four motions are shown in Fig. 5c, where the weighted uDop variations are quantified. For example, comparing the blue and the orange curves, the uDop velocity of motion 1 is around 0.05 to 0.1 m/s stronger than motion 3, because of the arm-swing. Comparing the blue and the purple curves, the RMS-DSs of motion 1 and motion 2 have the same trends, while motion 1 is stronger than motion 2 because the measured radial velocity of motion 1 is the vector sum of the torso velocity and the limb velocities. The motion 4 has the strongest uDop velocity, as the arm and leg swings are more pronounced when climbing stairs.

B. The effects of scattering paths and mirror targets

The motion 5 illustrated in Fig. 3b, is analyzed under three conditions, i.e., without the left wall, considering the left wall as a scattering clutter, and a mirror reflector. The time-Doppler results are shown in Fig. 6a to Fig. 6c, respectively. The three sub-figures share a similar profile in Doppler and envelope in uDop shift velocities. Compared with Fig. 6a, the main difference in Fig. 6b is the strong constant zero velocity due to the consideration of clutter. Fig. 6c is different from Fig. 6a because the mirror target fades the true target sometimes while enhancing it some other times, depending on the geometric position. However, the semantic feature is not obvious in the time-Doppler figures, because circular walking is much more complicated than the basic walking motions 1 to 4, where walking, orientation change, and environmental factors are integrated. The ND-PSD and the RMS-DS of the three scenarios of motion 5 are presented in Fig. 7a and Fig. 7b, respectively. Some important sites of circular walking

are denoted in Fig. 7c, where the circular track is denoted by the sites $S \rightarrow S_a \rightarrow S_b \rightarrow S_c \rightarrow S$.

The ND-PSD curves are consistent with the circular walking track. For example, the radial velocity changes as a sinusoid, resulting in a similar ND-PSD curve in Fig. 7a. The measured radial velocity becomes zero at site S_a and S_c because the human walk orientation is orthogonal to the radar radius orientation. In contrast, the measured radial velocity value becomes largest at site S_b, where the human walk orientation is parallel to the radius orientation. Comparing the black curve with the blue curve in Fig. 7a, the value of ND-PSD is relatively small with the scattering paths from the left wall, because the velocity of multipaths from the wall is zero. It is also worth mentioning that the two curves become similar when the subject walks along the track $S_c \rightarrow S$, because most of the scattering paths from the left wall are occluded. Comparing the black curve with the orange curve in Fig. 7a, the effects of the mirror target become random as the geometric position changes.

The curves of RMS-DS in Fig. 7b quantify the variances of the uDop. First of all, the two peaks of RMS-DS curves are observed for the three scenarios at sites S_a and S_c. This shows that the turning motion has the strongest uDop. The comparisons of the three curves remain consistent with the analysis of ND-PSD curves. The absolute value of the black curve is slightly smaller than the blue one because of the zero-velocity scattering paths. Because of the influence of the mirror target, the ghost target reduces the RMS-DS around $1\ m/s$ at the two peaks, while in several places the uDop features get enhanced, as a result, the orange curve becomes more fluctuated while flatter. Another interesting observation is the quantified uDop of the walking in motions 1 to 4 also maps with the circular walking. Recalling in motion 1, when walking in a line with the radar, the RMS-DS is 0.2 to $0.3\ m/s$. At the sites S and S_b, the walking orientation is in line with radar, and the blue curve in Fig. 7b is in this range, i.e., around $0.25\ m/s$. This implies the feasibility of utilizing RMS-DS for walking orientation identification.

IV. Conclusion

In this paper, we utilize the dynamic RT simulator from our previous work to characterize different human walking motions. Firstly, four walking motions in the anechoic chamber scenarios under conditions of walking, stepping, walking without arm-swing, and walking upstairs are exploited. Then, the circular walking in an anechoic chamber, scattering clutter, and mirror reflection scenarios are compared. In all the scenarios, the channel modeling parameters ND-PSD and RMS-DS are shown and compared with the conventional time-Doppler results. The ND-PSD and RMS-DS match with the information provided by conventional Doppler maps. Meanwhile, the channel parameters can provide more quantified information, e.g., the uDop strength difference due to the arm-swing by comparing motion 1 and 3, the influence of torso velocity on uDop velocity by comparing motion 1 and 2, and the uDop strength in normal walking and climbing by comparing motion 1 and 4. In mirror target scenarios, the channel parameters can provide semantic information when the time-Doppler results are fading, as in the example of motion 5. Those results show the channel parameters are also useful in characterizing human motions. This provides the feasibility of utilizing channel parameters to assist conventional radar images in training datasets.

References

[1] H. Yi, D. He, P. T. Mathiopoulos, B. Ai, J. M. García-Loygorri, J. Dou, and Z. Zhong, "Ray tracing meets terahertz: Challenges and opportunities," *IEEE Communications Magazine*, vol. 62, no. 2, pp. 40–46, 2024.

[2] Y. Liu, L. Wu, M. Alaee-Kerahroodi, and B. S. M. R, "A 3D indoor localization approach based on spherical wave-front and channel spatial geometry," in *2022 IEEE 12th Sensor Array and Multichannel Signal Processing Workshop (SAM)*, 2022, pp. 101–105.

[3] J. Le Kernec, F. Fioranelli, C. Ding, H. Zhao, L. Sun, H. Hong, J. Lorandel, and O. Romain, "Radar signal processing for sensing in assisted living: The challenges associated with real-time implementation of emerging algorithms," *IEEE Signal Processing Magazine*, vol. 36, no. 4, pp. 29–41, 2019.

[4] V. Chen, "Analysis of radar micro-Doppler with time-frequency transform," in *Proceedings of the Tenth IEEE Workshop on Statistical Signal and Array Processing (Cat. No.00TH8496)*, 2000, pp. 463–466.

[5] C. Wang, T. S. Kumar, W. De Raedt, G. Camps, H. Hallez, and B. Vanrumste, "Evaluation of different radar placements for food intake monitoring using deep learning," in *2023 IEEE Radar Conference (RadarConf23)*, 2023, pp. 1–6.

[6] Y. He, Y. Yang, Y. Lang, D. Huang, X. Jing, and C. Hou, "Deep learning based human activity classification in radar micro-doppler image," in *2018 15th European Radar Conference (EuRAD)*, 2018, pp. 230–233.

[7] N. K. Sichani, M. Ahmadi, E. Raei, M. Alaee-Kerahroodi, B. S. M. R., E. Mehrshahi, and S. A. Ghorashi, "Waveform selection for FMCW and PMCW 4D-imaging automotive radar sensors," in *2023 IEEE Radar Conference (RadarConf23)*, 2023, pp. 1–6.

[8] Y. Liu, W.-X. Long, R. Chen, L. Wu, and M. R. B. Shankar, "Vortex wavefront FMCW ISAC model: A blender-based evaluation," in *2023 IEEE 24th International Workshop on Signal Processing Advances in Wireless Communications (SPAWC)*, 2023, pp. 431–435.

[9] X. Ye, X. Yin, X. Cai, A. Pérez Yuste, and H. Xu, "Neural-network-assisted UE localization using radio-channel fingerprints in LTE networks," *IEEE Access*, vol. 5, pp. 12 071–12 087, 2017.

[10] F. Yu, M. Guo, P. Wang, G. Jing, J. Rodríguez-Piñeiro, and X. Yin, "A novel hybrid fingerprint-based indoor localization scheme with hierarchical training," in *2023 IEEE Globecom Workshops (GC Wkshps)*, 2023, pp. 1922–1927.

[11] C. Huang, A. F. Molisch, R. He, R. Wang, P. Tang, B. Ai, and Z. Zhong, "Machine learning-enabled LOS/NLOS identification for MIMO systems in dynamic environments," *IEEE Transactions on Wireless Communications*, vol. 19, no. 6, pp. 3643–3657, 2020.

[12] J. Rodríguez-Piñeiro, T. Domínguez-Bolaño, X. Cai, Z. Huang, and X. Yin, "Air-to-ground channel characterization for low-height UAVs in realistic network deployments," *IEEE Transactions on Antennas and Propagation*, vol. 69, no. 2, pp. 992–1006, 2021.

[13] Y. Liu, M. Ahmadi, J. Fuchs, M. Alaee-Kerahroodi, and M. R. Bhavani Shankar, "Dynamic indoor mmwave MIMO radar simulation: An image rendering-based approach," *IEEE Transactions on Antennas and Propagation*, pp. 1–1, 2024.

[14] F. Krebs, A. Meixner, I. Patzer, and T. Asfour, "The KIT bimanual manipulation dataset," in *IEEE/RAS International Conference on Humanoid Robots (Humanoids)*, 2021, pp. 499–506.

[15] N. Mahmood, N. Ghorbani, N. F. Troje, G. Pons-Moll, and M. J. Black, "AMASS: Archive of motion capture as surface shapes," in *International Conference on Computer Vision*, Oct. 2019, pp. 5442–5451.

[16] G. Pavlakos, V. Choutas, N. Ghorbani, T. Bolkart, A. A. A. Osman, D. Tzionas, and M. J. Black, "Expressive body capture: 3D hands, face, and body from a single image," in *Proceedings IEEE Conf. on Computer Vision and Pattern Recognition (CVPR)*, 2019, pp. 10 975–10 985.

[17] R. Sedman. (2017, October) How to calculate for every ray the total distance it has traveled from camera to emitter. [Online]. Available: https://blender.stackexchange.com/a/91760